Chapter 3

Prec: an iterative reconstruction method for correction of the Ewald Sphere

Peter A. Leong[a], Xuekui Yu[b], Z. Hong Zhou[b], Grant J. Jensen[c*]

[a]Department of Applied Physics, California Institute of Technology, 1200 E. California Boulevard, Pasadena, CA 91125, USA

[b]Department of Microbiology, Immunology & Molecular Genetics and The California NanoSystems Institute, 615 Charles E. Young Dr. S, BSRB 237; University of California Los Angeles, Los Angeles, CA 90095-7364, USA

[c]Division of Biology, California Institute of Technology, 1200 E. California Boulevard, Pasadena, CA 91125, USA

*To whom correspondence should be addressed: **jensen@caltech.edu**, 626-395-8827 (phone) 626-395-5730 (fax)

3.1 Abstract

To avoid the challenges of crystallization and the size limitations of NMR, it has long been hoped that single-particle cryo-electron microscopy (cryo-EM) would eventually yield atomically interpretable reconstructions. For the most favorable class of specimens (large icosahedral viruses), one of the key obstacles is curvature of the Ewald sphere, which leads to a breakdown of the projection theorem used by conventional 3D reconstruction programs. Here an iterative refinement reconstruction algorithm, *Prec*, is described that overcomes this limitation by averaging information from images recorded from different points of view, as are present in typical micrographs. *Prec* was implemented in the popular software packages IMIRS, EMAN, and Bsoft. In preliminary tests with both simple and multi-slice simulated images, *Prec* overcame the curvature problem even in the presence of noise. *Prec* was then used to refine the three recently published, ~ 4 Å resolution, icosahedral virus reconstructions from experimental cryo-EM images, but unfortunately no significant improvements in resolution were realized. Further simulations showed that limitations other than the Ewald sphere curvature problem must still be dominant in these experimental studies.

3.2 Introduction

X-ray crystallography and nuclear magnetic resonance spectroscopy (NMR) were the first techniques to reveal the atomic structures of biological macromolecules. Electron crystallography then followed, first on "two-dimensional" crystals (crystals one unit cell thick) (Henderson, Baldwin et al. 1990; Kuhlbrandt, Wang et al. 1994) and then on helical (tubular) crystals (Unwin 2005). To avoid the challenges of crystallization and the size limitations of NMR, it has long been hoped that single-particle cryo-electron microscopy (cryo-EM) would eventually also produce atomically interpretable maps. Steady progress towards this goal has been made (Frank 2002), led by reconstructions of large icosahedral viruses, whose 60-fold symmetry, size, and rigid architecture all facilitate precise image alignment. In just the past few months the structures of three such viruses — cytoplasmic polyhedrosis virus (CPV) (Yu, Jin et al. 2008), epsilon15 virus (ε15) (Jiang, Baker et al. 2008), and rotavirus (DLP) (Zhang, Settembre et al. 2008) — have been reconstructed to ~4 Å.

Previous analyses (DeRosier 2000; Jensen and Kornberg 2000; Zhang, Settembre et al. 2008) suggest that curvature of the Ewald sphere (or equivalently, the depth of field (Zhou and Chiu 1993)) may have been one of the principal resolution limitations in these recent studies. Conventional methods assume that EM images are true projections, but in fact they are not: the information delivered by the microscope is actually a mixture of information belonging to a curved surface within the three-dimensional (3D) Fourier transform of the specimen called the Ewald sphere. The mixing occurs when the complex electron wave functions are measured by the CCD or film to produce real

images. The severity of the problem increases with specimen thickness, resolution, and electron wavelength.

A method for recovering the full, complex electron wavefunction from focal series was proposed by Schiske in 1968 (Schiske 1968). Further discussion then followed through 1990, when the method was re-proposed using a different, more intuitive approach (Van Dyck and Op de Beeck 1990). Saxton, who referred to this class of approaches as the paraboloid method (PM), later showed it to be equivalent to the original (Saxton 1994). More recently, the problem was discussed in the context of 3D reconstruction by DeRosier, who outlined four basic strategies to recover all the unique Fourier coefficients by merging focal pairs, images at different tilt angles, or images of ordered (crystalline or helical) objects in reciprocal space (DeRosier 2000). A different idea for addressing the problem in real space was proposed by Jensen and Kornberg (Jensen and Kornberg 2000), followed by additional analyses and suggestions by Wan et al. (Wan, Chiu et al. 2004).

Unfortunately, none of these efforts produced an efficient, practical program ready for use within the software packages available for the calculation of high-resolution reconstructions of viruses from experimental images. Here we describe a version of the PM we call *Prec* (for paraboloid reconstruction), which iteratively retrieves the information lost due to curvature of the Ewald sphere, and its implementation into three modern software packages. First, two Cartesian-coordinate-based versions of *Prec* were implemented in Bsoft (Heymann 2001) and EMAN (Ludtke, Baldwin et al. 1999) to

facilitate development and testing. Next a cylindrical-coordinate-based version was implemented in IMIRS (Liang, Ke et al. 2002), a commonly used software package for high-resolution icosahedral reconstructions which exploits the advantages of cylindrical coordinates and Fourier-Bessel transforms (Klug, Crick et al. 1958). Using simulated images, we show that all three implementations relieve the resolution limitations of the Ewald sphere, but surprisingly do not substantially improve the resolution of the three recent near-atomic-resolution reconstructions from experimental cryo-EM images. We conclude that other factors (besides the curvature problem) are still principally limiting. During the course of this effort, Wolf et al. (Wolf, DeRosier et al. 2006) implemented a comparable version of the PM in the also popular, Cartesian-coordinate-based FREALIGN package (Grigorieff 2007) and tested its efficacy on simulated images. Differences in the algorithms and performance of the *Prec* and FREALIGN implementations are discussed.

3.3 Results

3.3.1 The Ewald Curvature Problem and Symbols Used — To introduce needed symbols, we will follow DeRosier's derivation of the effects of the Ewald sphere curvature closely (DeRosier 2000), except that here all Fourier coefficients F are complex and amplitude contrast is included explicitly. Beginning first with the effect of a sample on an incident electron wave and its weak-phase approximation,

$$\frac{A_t(x)}{A_0} = e^{-(\alpha+i\beta)\rho(x)} \approx 1-(\alpha+i\beta)\rho(x) \qquad (1)$$

where $A_t(x)$ is the transmitted wave, A_0 is the incoming wave, α is the amplitude contrast value, $\beta = \sqrt{1-\alpha^2}$ is the phase contrast value (Erickson and Klug 1971), $\rho(x)$ is the density of the sample, and i is an imaginary number with magnitude 1; the diffracted wave $F(X)$ takes the form

$$F(X) = FT[1-(\alpha+i\beta)\rho(x)] = \delta(X) - (\alpha+i\beta)F_\rho(X) \tag{2}$$

where $F_\rho(X)$ is the Fourier transform (FT) of our sample density.

Considering the sum of a single, symmetric pair of diffracted beams represented by Fourier coefficients F_L and F_R on an Ewald sphere (Figure 3-1), whose additional path length through the lens with respect to the unscattered beam adds an additional phase shift of $e^{i\chi}$, we have:

$$F(X) = \delta(X) - (\alpha+i\beta)F_L e^{i\chi}\delta(X+X_a) - (\alpha+i\beta)F_R e^{i\chi}\delta(X-X_a) \tag{3}$$

where χ is the wave aberration function at X_a and is defined as

$$\chi(s) = \tfrac{\pi}{2} C_s \lambda^3 s^4 - \pi \Delta f \, \lambda s^2 \tag{4}$$

in which λ is the electron wavelength, s is the spatial frequency, C_s is the spherical aberration coefficient, and Δf is the defocus.

The interference of these beams will produce a single complex fringe with a periodicity of $\frac{1}{X_a}$ whose amplitude, $\sigma(x)$, will be

$$\sigma(x) = FT^{-1}[F(X)] = 1 - (\alpha + i\beta)F_L e^{i\chi} e^{-2\pi i x X_a} - (\alpha + i\beta)F_R e^{i\chi} e^{2\pi i x X_a} \tag{5}$$

The intensity of the wave is recorded as our image

$$\begin{aligned} |\sigma(x)|^2 \approx 1 &- [(\alpha + i\beta)F_L e^{i\chi} + (\alpha - i\beta)F_R^* e^{-i\chi}]e^{-2\pi i x X_a} \\ &- [(\alpha + i\beta)F_R e^{i\chi} + (\alpha - i\beta)F_L^* e^{-i\chi}]e^{2\pi i x X_a} \end{aligned} \tag{6}$$

where the F^2 terms can be ignored due to the weak phase approximation.

The FT of our image $F_{obs}(X)$ is then

$$\begin{aligned} F_{obs}(X) = \delta(X) &- [(\alpha + i\beta)F_L e^{i\chi} + (\alpha - i\beta)F_R^* e^{-i\chi}]\delta(X + X_a) \\ &- [(\alpha - i\beta)F_L^* e^{-i\chi} + (\alpha + i\beta)F_R e^{i\chi}]\delta(X - X_a) \end{aligned} \tag{7}$$

We see that $F_{R_{obs}}$, the observed Fourier value on the right side at $X = X_a$, is

$$F_{R_{obs}} = -F_L^*(\alpha - i\beta)e^{-i\chi} - F_R(\alpha + i\beta)e^{i\chi} \tag{8}$$

Because of the curvature of the Ewald sphere, F_L and F_R are not a Friedel pair (i.e., not complex conjugates), but rather independent Fourier coefficients, mixed by the process of

image formation. Thus conventional methods, which treat $F_{R_{obs}}$ as if it were the sum of a Friedel pair F_L and F_R, do progressively worse as F_L and F_R diverge at higher resolutions.

3.3.2 The Paraboloid Method in the Context of 3D Reconstruction — The original Fourier coefficients can be recovered by averaging information from multiple images, which each contain different combinations of the unique coefficients. First, images are corrected for the contrast transfer function (CTF). This is performed by multiplying each term F_{obs} by $-(\alpha - i\beta)e^{-i\chi}$. Unlike conventional CTF corrections, where values around CTF zeros are discarded, here there is no such requirement, since this "complex" CTF-correction (cCTF) is a multiplication by a factor of magnitude 1 rather than a division by a number potentially close to zero. Thus $F_{R_{corr}}$, the cCTF-corrected coefficient on the right side, is

$$F_{R_{corr}} = -F_{R_{obs}}(\alpha - i\beta)e^{-i\chi} = F_R + F_L^*(\alpha - i\beta)^2 e^{-i2\chi} \tag{9}$$

Because each $F_{R_{corr}}$ is the sum of the correct F_R and a phase-shifted, complex-conjugated F_L, at this point it becomes clear how by averaging $F_{R_{corr}}$ from a number of different images, each measuring the same F_R but different F_Ls, the F_Rs will add coherently but the sum of F_Ls will diminish in comparison. At low resolution, however, where $F_L^* \approx F_R$,

$$F_{R_{obs}} \approx -F_R(\alpha - i\beta)e^{-i\chi} - F_R(\alpha + i\beta)e^{i\chi} = -2F_R(\alpha\cos\chi - \beta\sin\chi) \tag{10}$$

The cCTF correction then leads to wrong values

$$F_{R_{corr}} = F_R + F_R(\alpha - i\beta)^2 e^{-i2\chi} \tag{11}$$

since χ does not vary quickly, causing the second terms to also add coherently and introduce a significant error. Thus at low resolution, it is better to use the simpler, real CTF correction (rCTF), where F_{obs} is divided by the factor $-2(\alpha\cos\chi - \beta\sin\chi)$. A practical transition point can be found as the spatial frequency at which the cCTF-corrected and the rCTF-corrected reconstructions match best (as demonstrated in the CPV reconstruction below).

After CTF-correcting the raw images, the often described paraboloid method (PM) places the F_{corr} values in their correct position in Fourier space on the Ewald sphere:

$$F_{R_{PM}} = \tfrac{1}{N}\sum_k^N F_{R^k_{corr}} = \tfrac{1}{N}\sum_k^N F_{R_k} + \tfrac{1}{N}\sum_k^N F^*_{L_k}(\alpha - i\beta)^2 e^{-i2\chi_k} \tag{12}$$

$$F_{L_{PM}} = \tfrac{1}{N}\sum_k^N F_{L^k_{corr}} = \tfrac{1}{N}\sum_k^N F_{L_k} + \tfrac{1}{N}\sum_k^N F^*_{R_k}(\alpha - i\beta)^2 e^{-i2\chi_k} \tag{13}$$

where N is the total number of images (indexed by k) which contribute to each point.

3.3.3 The Prec *Algorithm* — In essence, the PM therefore "splits" the observed values F_{obs} into estimates of F_R and F_L by averaging information from a set of images. Once initial estimates are obtained, they can be refined through iteration, since knowledge of any particular coefficient will affect how all the sums it is involved in should be split. In *Prec*'s iterative refinement loop, each F_{obs} of each image is compared to the expected ("calculated") value $F_{R_{calc}}$ that is obtained by combining Ewald sphere-related Fourier coefficients from a previous reconstruction:

$$F_{R_{calc}} = F_{R_j} + F^*_{L_j}(\alpha - i\beta)^2 e^{-i2\chi} \tag{14}$$

where the index j represents the j^{th} iteration of the reconstruction. The difference between the CTF-corrected observed value for image k and this calculated value is stored as the "error" $2F_{\Delta_k}$:

$$F_{R^k_{corr}} - F_{R^k_{calc}} = 2F_{\Delta_k} \tag{15}$$

Half of these errors are then added as a refinement to the Fourier component on the right:

$$F_{R_{j+1}} = F_{R_j} + \tfrac{1}{N}\sum_k^N F_{\Delta_k} \tag{16}$$

The correction can also be immediately added to the left side:

$$F^*_{L_{j+1}}(\alpha - i\beta)^2 e^{-i2\chi} = F^*_{L_j}(\alpha - i\beta)^2 e^{-i2\chi} + F_\Delta \tag{17}$$

which, after rotation, complex conjugation, and summation of corrections, simplifies to:

$$F_{L_{j+1}} = F_{L_j} + \tfrac{1}{N}\sum_k^N F^*_{\Delta_k}(\alpha - i\beta)^2 e^{-i2\chi_k} \tag{18}$$

In the special (initial) case where the reconstruction to be refined consists completely of a set of zeroes, the calculated value, $F_{R_{calc}}$, is also zero and thus the correction applied to the left and right Fourier components (F_{R_0} and F_{L_0}) can be shown to be equivalent to the PM, scaled by a simple factor of $\frac{1}{2}$:

$$F_{R^k_{corr}} = 2F_{\Delta_k} \tag{19}$$

$$F_{R_0} = \tfrac{1}{N}\sum_k^N F_{\Delta_k} = \tfrac{1}{N}\sum_k^N \tfrac{1}{2} F_{R^k_{corr}} = \tfrac{1}{2} F_{R_{PM}} \tag{20}$$

$$\begin{aligned} F_{L_0} &= \tfrac{1}{N}\sum_k^N F^*_{\Delta_k}(\alpha - i\beta)^2 e^{-i2\chi_k} = \tfrac{1}{N}\sum_k^N \tfrac{1}{2} F^*_{R^k_{corr}}(\alpha - i\beta)^2 e^{-i2\chi_k} \\ &= \tfrac{1}{N}\sum_k^N \tfrac{1}{2} F_{L^k_{corr}} = \tfrac{1}{2} F_{L_{PM}} \end{aligned} \tag{21}$$

The effect of iterating turns out to be small, however. Take for example any Fourier coefficient F_{R_0} and the contributions to it:

$$F_{R_0} = \frac{1}{N}\sum_{k}^{N} F_{R_k} + \frac{1}{N}\sum_{k}^{N} F_{L_k}^{*}(\alpha - i\beta)^2 e^{-i2\chi_k} \tag{22}$$

where N is the number of images that measured F_R.

This can be recast as

$$F_{R_0} \approx \overline{F}_R + \varepsilon \tag{23}$$

where $\overline{F}_R$ is the average F_{R_k} and ε is the residual error which consists of the average of the $F_{L_k}(\alpha - i\beta)^2 e^{-i2\chi_k}$ terms, which is a random walk with step size of approximately $\overline{|F_{L_k}|}$. As such, after the first refinement cycle the residual error falls off as $\sim\frac{1}{\sqrt{N}}$, so that for large numbers of images, only small improvements can be expected from iteration.

3.3.4 Implementation of the Prec *Algorithm* — Three versions of *Prec* were implemented, one each in the software packages Bsoft, IMIRS, and EMAN, which each have all the functionality required to produce high-resolution reconstructions from raw cryo-EM images. While the mathematical theory is as described above, key differences exist in how the interpolations are handled in the different coordinate systems. Bsoft and EMAN use a Cartesian coordinate system. Starting with raw cryo-EM images, the Bsoft and EMAN implementations of *Prec* begin by calculating the images' 2D FTs, multiplying

them by the cCTF, and then calculating the "z-" coordinate (height up the Ewald sphere) for each Fourier coefficient. Taking into account the projection direction, the coefficients from the image are then added to the nearest corresponding lattice points of the "reconstruction" 3D FT with appropriate phase factors. In the Bsoft version, the standard interpolation procedure with weight $w = 1 - d$ (where d is distance in pixels from the measurement to the 3D lattice point) is used. In the EMAN version, any of its various built-in interpolation procedures can be used. After all the data are added to the "reconstruction" 3D FT, each amplitude is divided by the total weight of all the measurements that contributed, and a density map is produced through an inverse 3D FT. Refinement cycles, implemented in Bsoft, loop through each coefficient of each corrected image transform. The expected value is calculated by summing the coefficients at the nearest corresponding lattice points of the 3D FT of the current reconstruction with appropriate phase factors and complex conjugation. Half the difference between this expected value and the (CTF-corrected) observed value is added to each contributing coefficient.

A different version of *Prec* was implemented within IMIRS. IMIRS uses a cylindrical coordinate system for the reconstruction process where the 3D reconstruction and its FT are expressed as expansions of cylinder functions, as proposed by Klug et al. (Klug, Crick et al. 1958). We follow the notation used by Crowther et al. (Crowther, Derosier et al. 1970). The 2D FTs of the raw images are calculated and multiplied by the cCTF as before. The 3D FT of the object is represented in cylindrical coordinates, Z, R, and Φ. The Ewald sphere of measurements recorded in each image will in general intersect each

ring of coordinates in two places. For each intersection of an image Ewald sphere and a ring of the 3D FT, a Fourier coefficient for that location is estimated from the pixels of the FT of the image through bilinear interpolation. Once all the estimates on a particular ring have been calculated, all of them are used to determine the cylindrical expansion terms, $G_n(R,Z)$ through a least-squares fit which differs from the conventional IMIRS reconstruction in that the magnitude of the cCTF term is 1 and therefore is not a factor in the weighting of terms. A Fourier-Bessel transform is used next to obtain the $g_n(r,Z)$ terms, which are then used to generate the density map.

Because in this case the F_L that pairs with each F_R of a randomly spaced intersection of an image Ewald sphere and a Fourier ring does not generally fall upon any ring, a 3D nearest neighbor interpolation was required to estimate its value. Our tests (see below) suggested that the losses due to this less-accurate nearest-neighbor interpolation outweighed the gains obtained by iteration, so that iteration of the cylindrical-coordinate-based version of *Prec* is not recommended. In addition, astigmatism correction capabilities were added to both the conventional and *Prec* IMIRS reconstruction programs to accommodate the DLP dataset (see below).

3.3.5 Tests on Simulated Images — In order to explore the problems caused by Ewald sphere curvature and verify *Prec's* ability to solve them, a large number of images of the moderate-sized (~ 300 Å diameter) foot-and-mouth disease virus (FMDV) (Fry, Acharya et al. 1993) were simulated with different methodologies, voltages, and signal-to-noise ratios. A complete pdb was generated using the VIPERdb (Shepherd, Borelli et al. 2006)

and then its density was sampled to produce a reference volume using a modified version of *bgex* of the Bsoft package. Two types of simulated images were then calculated. The first, "Ewald projection" method produced images by simply summing Fourier coefficients on Ewald spheres using equation 8 and a complete 1D Whittaker-Shannon interpolation (Whittaker 1915; Shannon 1949) in the Z direction, followed by an inverse 2D FT. In order to produce a second, methodologically independent and more accurate set of simulated images, we used the multi-slice algorithm (Cowley and Moodie 1957). This well-established method tracks the dynamic scattering events that are increasingly important for thick samples, and was implemented in Bsoft by Heymann and Jensen with the assumption that scattering is completely elastic (*manuscript in preparation*). The sample is considered as a stack of equally thick slices. The effect of each slice on an incident plane wave is tracked by multiplying the slice's projected density (treated as a phase grating) with the wave function. The propagation of the wave between slices is calculated by convolution with a "propagator" function, so that the effects of Ewald sphere curvature arise naturally as the incident wave passes through the slices. After interaction with the final slice, the multi-slice image is generated by convolving the exit wave function with a complex contrast transfer function representing the lens.

As a first test, the simpler Ewald projections with varying acceleration voltages were used to study the effect of the electron wavelength on the maximum achievable resolution. Six data sets of 5000 Ewald projections each, with acceleration voltages of 15, 25, 50, 100, 200, and 300 kV, respectively, were calculated. FMDV reconstructions were then calculated from each data set using the conventional reconstruction programs

in Bsoft, IMIRS, and EMAN, which do not correct for curvature of the Ewald sphere. The resolution of each reconstruction was measured by its correlation with the original reference density map in Fourier shells (FSC) and confirmed visually (Figure 3-2, Bsoft results only). The large number of images ensured that Fourier space was well sampled. The expected increase in resolution as a function of voltage demonstrated the Ewald sphere curvature problem.

Analogous reconstructions of the 15 kV data set were then performed with Bsoft, IMIRS, and EMAN implementations of *Prec*. All three programs completely overcame the effects of Ewald sphere curvature. Because in this context the exact wave aberration values χ used to simulate the images in Bsoft could only be estimated by interpolation in the IMIRS coordinate system, the *Prec* in IMIRS reconstruction failed to reach all the way to Nyquist frequency, but instead was eventually limited by the rate of change of χ to ~ 3 Å resolution. In practice, where voltages much higher than 15 kV are used, this behavior of χ will not be limiting for either program.

Next the effects of smaller numbers of images and noise were explored using multi-slice images. Five-thousand FMDV images were again calculated, this time using Peach (Leong, Heymann et al. 2005), a distributed computation system, to meet the heavier computational demands of the multi-slice algorithm. A voltage of 15 kV was again assumed to ensure that the Ewald sphere curvature limitations would be manifest well before Nyquist frequency. Multiple sets of images with different signal-to-noise-ratios (SNRs) were then produced by first calculating the standard deviation of the raw multi-

slice image (σ_{image}), and then adding random Gaussian noise with standard deviation σ_{noise} to each pixel such that $(\frac{\sigma_{image}}{\sigma_{noise}})^2$ was equal to the desired SNR.

To confirm the presence of the Ewald sphere curvature problem in the multi-slice images, conventional reconstructions were produced from 25, 50, 100, 250, 500, 1000, 2500, and 5000 images, respectively, all with a SNR of 0.1, using the conventional *reconstruct* program in IMIRS. The reconstructions were again limited to ~ 4.2 Å, regardless of how many images were included (data not shown, except for the 5000-image reconstruction curve, which is part of the set described next). Application of the Bsoft, IMIRS, and EMAN versions of *Prec* removed the limitation (Figure 3-3, IMIRS results only), although the IMIRS reconstructions were again limited to ~ 3 Å resolution by the CTF-correction interpolation problem explained earlier.

In order to test how robust *Prec*'s refinement algorithm is to the presence of noise, similar reconstructions were calculated from 5000-image data sets with SNR ratios of 0.05, 0.01, and 0.001. While the resolutions of the corresponding reconstructions progressively decreased with increasing noise, in every case *Prec* clearly overcame the basic problem of Ewald sphere curvature (Figure 3-3). Further improvements were not realized by second or third iterations of *Prec* (the cylindrical-coordinate-based IMIRS version), probably for the reason described in Section 2.4.

3.3.6 Application to the CPV, ε15, and DLP reconstructions — Although several groups have proposed solutions to the Ewald sphere limitation in the context of complex wavefront recovery (Saxton 1994), none to our knowledge have shown a successful correction in a 3D reconstruction from experimental data. The recent publication of three near-atomic resolution (~ 4 Å) reconstructions of large (~ 700-Å diameter) viruses presents an opportunity to do so. According to Jensen and Kornberg's envelope function (Jensen and Kornberg 2000), half of the signal in a conventional reconstruction of such a large virus at 300 kV would be lost due to curvature of the Ewald sphere by 3.5 Å resolution. Likewise, DeRosier's formula (DeRosier 2000) predicts that the curvature problem in this same situation would become significantly limiting by 3.3 Å resolution. Thus as a further test of *Prec*, it was next used to refine the experimental reconstructions of CPV, ε15, and DLP.

CPV is a 750 Å diameter dsRNA virus in the *Reoviridae* family. Using the same cryo-EM images, two different 3D reconstructions were obtained using *Prec* and, for comparison, the conventional *IMIRS* reconstruction program. While in the previous tests of *Prec* with simulated images, only the cCTF-correction was used, in order to optimize this experimental reconstruction of CPV at all spatial frequencies, the low frequency Fourier coefficients of the (cCTF-corrected) *Prec* reconstruction were replaced with those from the conventional (rCTF-corrected) *reconstruct* version, as discussed above in conjunction with equation 10. The transition point was chosen as the spatial frequency where the two reconstructions matched best (~ 17 Å, Figure 3-4).

Disappointingly, the *Prec* reconstruction of CPV was not significantly better than the conventional. By visual inspection, the *Prec* reconstruction looked just slightly higher resolution in several locations, but not conclusively so (Figure 3-4a–i). Because the same images and particle parameters (defocus, origin, orientation) were used in these reconstructions, all the differences were due to *Prec*'s correction for Ewald sphere curvature. To compare the resolutions of the two maps quantitatively, the CPV cryo-EM image dataset was split into halves and independent "half-maps" were generated by *Prec* and then again by the conventional IMIRS *reconstruct* program. After all four maps were normalized and a soft spherical mask was imposed to remove noise inside the capsid shell, FSC curves were calculated (Ludtke, Baldwin et al. 1999)(Figure 3-4j). While the large spaces around the turrets and within the capsid shell devoid of protein reduce correlation and make it difficult to relate these FSC curves to the actual interpretability of the map, again these curves suggested that the *Prec* map might have had just slightly higher resolution at frequencies where the signal seemed reliable (i.e., $< \sim 1/6$ Å^{-1}), but not significantly. Similarly, the experimental reconstructions of the 700 and 710 Å diameter ε15 and DLP viruses calculated with the EMAN and IMIRS programs, respectively, were also only marginally if at all improved by refinement with *Prec* (data not shown).

In order to explore why more significant improvements were not realized, a single set of images were simulated of the equally large (754 Å diameter) reovirus core (Reinisch, Nibert et al. 2000) at the same voltage used in the experiments (300 kV). In this case applying the multi-slice algorithm was not computationally practical, so only Ewald

projections were used. After a conventional (EMAN) reconstruction was calculated from these simulated images, FSC analysis indicated a resolution of ~ 2.5 Å, much better than predicted by either Jensen and Kornberg's envelope or DeRosier's formula. Because the experimental reconstructions of CPV, ε15, and DLP had significantly worse resolution, we conclude that other resolution limitations besides the Ewald curvature problem must still be experimentally dominant. *Prec* in either Bsoft or EMAN again alleviated the problem in this simulated context as expected (Figure 3-5, EMAN results only).

3.4 Discussion

Here we have described *Prec*, an iterative algorithm based on the oft-described PM that corrects for curvature of the Ewald sphere in 3D reconstructions. Three versions were implemented: two Cartesian-coordinate-based versions in the software packages Bsoft (where multi-threading was also introduced) and EMAN, and a cylindrical-coordinate-based version in IMIRS. To test *Prec*, numerous images of a moderately sized virus were simulated in two different ways, namely simple Ewald projection and the more sophisticated multi-slice method. All three versions of *Prec* corrected for the curvature problem in reconstructions from both types of simulated images, even in the presence of noise greater than that found in typical experimental images. *Prec* was then used to refine the experimental reconstructions of CPV, ε15, and DLP from cryo-EM images. Disappointingly, none of these experimental reconstructions were significantly improved. To explain this result, a single set of images were simulated of a similarly large virus with the same imaging parameters used in the experimental reconstructions. Reconstructions from these simulated images showed that, contrary to expectations, the

Ewald curvature did not become severely limiting until ~ 2.5 Å resolution. Thus other factors besides Ewald sphere curvature are still the predominant resolution limitation even in these high-resolution experimental reconstructions. As the size of reconstructed viruses, the number and quality of images that are included in reconstructions, and the precision to which those images can be mutually aligned continue to increase, Ewald curvature correction will nevertheless eventually become essential.

During the course of this project, Wolf et al. implemented a Cartesian-coordinate-based version of the PM similar to ours but in the FREALIGN package and with minor differences in the weighting factors involved in CTF correction (Wolf, DeRosier et al. 2006). These differences allowed a single CTF correction strategy to be used throughout the resolution range rather than the combination of real and complex CTF corrections used by *Prec* at low and high spatial frequencies, respectively. Wolf et al. further proposed an iterative, "reference-based insertion" method similar to our iterative algorithm, and tested it on simulated images, but reported that under conditions of low signal, iteration decreased FSCs. Here the Cartesian-coordinate- but not the cylindrical-coordinate-based version of *Prec* realized slight gains through iteration, even in the presence of noise, but the specific reasons for the difference remain unclear.

The cylindrical-coordinate-based version of *Prec* has two major advantages in comparison to the Cartesian implementations (Bsoft, EMAN, and FREALIGN). First, the cylindrical expansions allow all the measurements on a particular ring to be used to sample specific Fourier coefficients (Crowther, Derosier et al. 1970). Second, the

cylindrical-coordinate-based *Prec* program is much faster and requires less memory. Our CPV reconstructions from over twelve thousand 1k x 1k images required less than a day on a single-processor personal PC and used less than 2 Gbytes of memory. In contrast, even the multi-threaded and distributed versions of the Cartesian-based *Prec* in Bsoft and EMAN would have required a prohibitive ~ 20 and ~ 16 Gbytes of memory, respectively, and approximately 10 times more computing power to match the computation times of IMIRS. Likewise, Equation 5 of (Grigorieff 2007) suggests that FREALIGN would need 30 Gbytes of memory for such images.

The programs created for this project are freely available at www.jensenlab.caltech.edu.

3.5 Acknowledgements

We thank Andy Rawlinson, Bernard Heymann, Bill Tivol, Dylan Morris, Yuyao Liang, Wong Hoi Hui, Xiaokang Zhang, Weimin Wu, Wen Jiang and Nikolaus Grigorieff for helpful discussions about Ewald sphere curvature and the manuscript as well as the Bsoft, IMIRS, and EMAN packages and for providing experimental data. This work was supported in part by NIH grants R01 AI067548 and P50 GM082545 to GJJ and R01 GM071940, CA094809 and AI069015 to ZHZ; DOE grant DE-FG02-04ER63785 to GJJ; a Searle Scholar Award to GJJ; the Beckman Institute at Caltech; and gifts to Caltech from the Parsons Foundation and Agouron Institute. Access to the 4-node and 8-node Sun Fire X4600 computers, located at the California Institute of Technology, was provided by the Center for Advanced Computing Research.

3.6 References

Cowley, J. M. and A. F. Moodie (1957). "The Scattering of Electrons by Atoms and Crystals .1. a New Theoretical Approach." Acta Crystallographica **10**(10): 609−619.

Crowther, R. A., D. J. Derosier, et al. (1970). "Reconstruction of 3 Dimensional Structure from Projections and Its Application to Electron Microscopy." Proceedings of the Royal Society of London Series A-Mathematical and Physical Sciences **317**(1530): 319−340.

DeRosier, D. J. (2000). "Correction of high-resolution data for curvature of the Ewald sphere." Ultramicroscopy **81**(2): 83−98.

Erickson, H. P. and A. Klug (1971). "Measurement and Compensation of Defocusing and Aberrations by Fourier Processing of Electron Micrographs." Philosophical Transactions of the Royal Society of London Series B-Biological Sciences **261**(837): 105−118.

Frank, J. (2002). "Single-particle imaging of macromolecules by cryo-electron microscopy." Annual Review of Biophysics and Biomolecular Structure **31**: 303−319.

Fry, E., R. Acharya, et al. (1993). "Methods Used in the Structure Determination of Foot-and-Mouth-Disease Virus." Acta Crystallographica Section A **49**: 45−55.

Grigorieff, N. (2007). "FREALIGN: High-resolution refinement of single particle structures." Journal of Structural Biology **157**(1): 117−125.

Henderson, R., J. M. Baldwin, et al. (1990). "Model for the Structure of Bacteriorhodopsin Based on High-Resolution Electron Cryomicroscopy." Journal of Molecular Biology **213**(4): 899−929.

Heymann, J. B. (2001). "Bsoft: Image and molecular processing in electron microscopy." Journal of Structural Biology **133**(2−3): 156−169.

Jensen, G. J. and R. D. Kornberg (2000). "Defocus-gradient corrected back-projection." Ultramicroscopy **84**(1−2): 57−64.

Jiang, W., M. L. Baker, et al. (2008). "Backbone structure of the infectious epsilon 15 virus capsid revealed by electron cryomicroscopy." Nature **451**(7182): 1130−1134.

Klug, A., F. H. C. Crick, et al. (1958). "Diffraction by Helical Structures." Acta Crystallographica **11**(3): 199−213.

Kuhlbrandt, W., D. N. Wang, et al. (1994). "Atomic Model of Plant Light-Harvesting Complex by Electron Crystallography." Nature **367**(6464): 614−621.

Leong, P. A., J. B. Heymann, et al. (2005). "Peach: A simple perl-based system for distributed computation and its application to cryo-EM data processing - Ways & means." Structure **13**(4): 505−511.

Liang, Y. Y., E. Y. Ke, et al. (2002). "IMIRS: a high-resolution 3D reconstruction package integrated with a relational image database." Journal of Structural Biology **137**(3): 292−304.

Ludtke, S. J., P. R. Baldwin, et al. (1999). "EMAN: Semiautomated software for high-resolution single-particle reconstructions." Journal of Structural Biology **128**(1): 82−97.

Pettersen, E. F., T. D. Goddard, et al. (2004). "UCSF chimera - A visualization system for exploratory research and analysis." Journal Of Computational Chemistry **25**(13): 1605−1612.

Reinisch, K. M., M. Nibert, et al. (2000). "Structure of the reovirus core at 3.6 angstrom resolution." Nature **404**(6781): 960−967.

Saxton, W. O. (1994). "What Is the Focus Variation Method - Is It New - Is It Direct." Ultramicroscopy **55**(2): 171−181.

Schiske, P. (1968). "Zur Frage der Bildrekonstruktion durch Fokusreihen." Proc. 4th Eur. Conf. on Electron Microscopy Rome.

Shannon, C. E. (1949). "Communication in the Presence of Noise." Proceedings of the Institute of Radio Engineers **37**(1): 10−21.

Shepherd, C. M., I. A. Borelli, et al. (2006). "VIPERdb: a relational database for structural virology." Nucleic Acids Research **34**: D386−D389.

Unwin, N. (2005). "Refined structure of the nicotinic acetylcholine receptor at 4 angstrom resolution." Journal of Molecular Biology **346**(4): 967−989.

Van Dyck, D. and M. Op de Beeck (1990). "New direct methods for phase and structure retrieval by HREM." Proc. 12th Int. Congr. on Electron Microscopy Seattle.

Wan, Y., W. Chiu, et al. (2004). "Full contrast transfer function correction in 3D cryo-EM reconstruction." IEEE Proceedings of ICCCAS 2004 Chengdu, Sichuan, China.

Whittaker, E. T. (1915). "On the Functions which are Represented by the Expansion of Interpolation Theory." Proceedings of the Royal Society of Edinburgh **35**: 181−194.

Wolf, M., D. J. DeRosier, et al. (2006). "Ewald sphere correction for single-particle electron microscopy." Ultramicroscopy **106**(4−5): 376−382.

Yu, X. K., L. Jin, et al. (2008). "3.88 angstrom structure of cytoplasmic polyhedrosis virus by cryo-electron microscopy." Nature **453**(7193): 415−419.

Zhang, X., E. Settembre, et al. (2008). "Near-atomic resolution using electron cryomicroscopy and single-particle reconstruction." Proceedings of the National Academy of Sciences of the United States of America **105**(6): 1867−1872.

Zhou, Z. H. and W. Chiu (1993). "Prospects for using an IVEM with a FEG for imaging macromolecules towards atomic resolution." Ultramicroscopy **49**(1−4): 407−416.

3.7 Figures

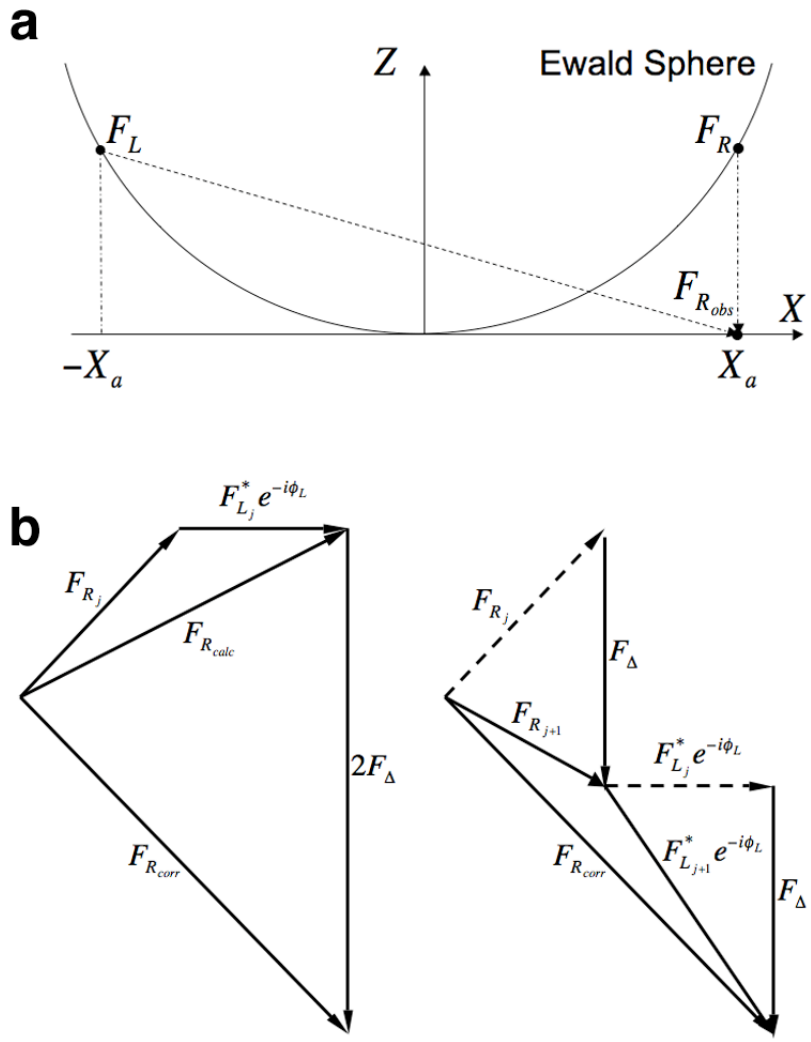

Figure 3-1. **The Ewald sphere and *Prec* algorithm.** (a) Fourier coefficients in the transforms of electron microscope images ($F_{R_{obs}}$) are actually combinations of coefficients (F_L and F_R) that lie on a spherical surface through the 3D transform of the specimen called the Ewald sphere. (b) *Prec* iteratively recovers the independent values of these coefficients by comparing CTF-corrected observations ($F_{R_{corr}}$) with the calculated sum ($F_{R_{calc}}$) that would have been expected from the right (F_{R_j}) and left (F_{L_j}) terms of some previous reconstruction, with appropriate phase factors $e^{i\phi_L} = (\alpha + i\beta)^2 e^{i2\chi}$. Half the difference ($F_\Delta$) is then added to F_{R_j} and F_{L_j} to produce the next iteration ($F_{R_{j+1}}$ and $F_{L_{j+1}}$).

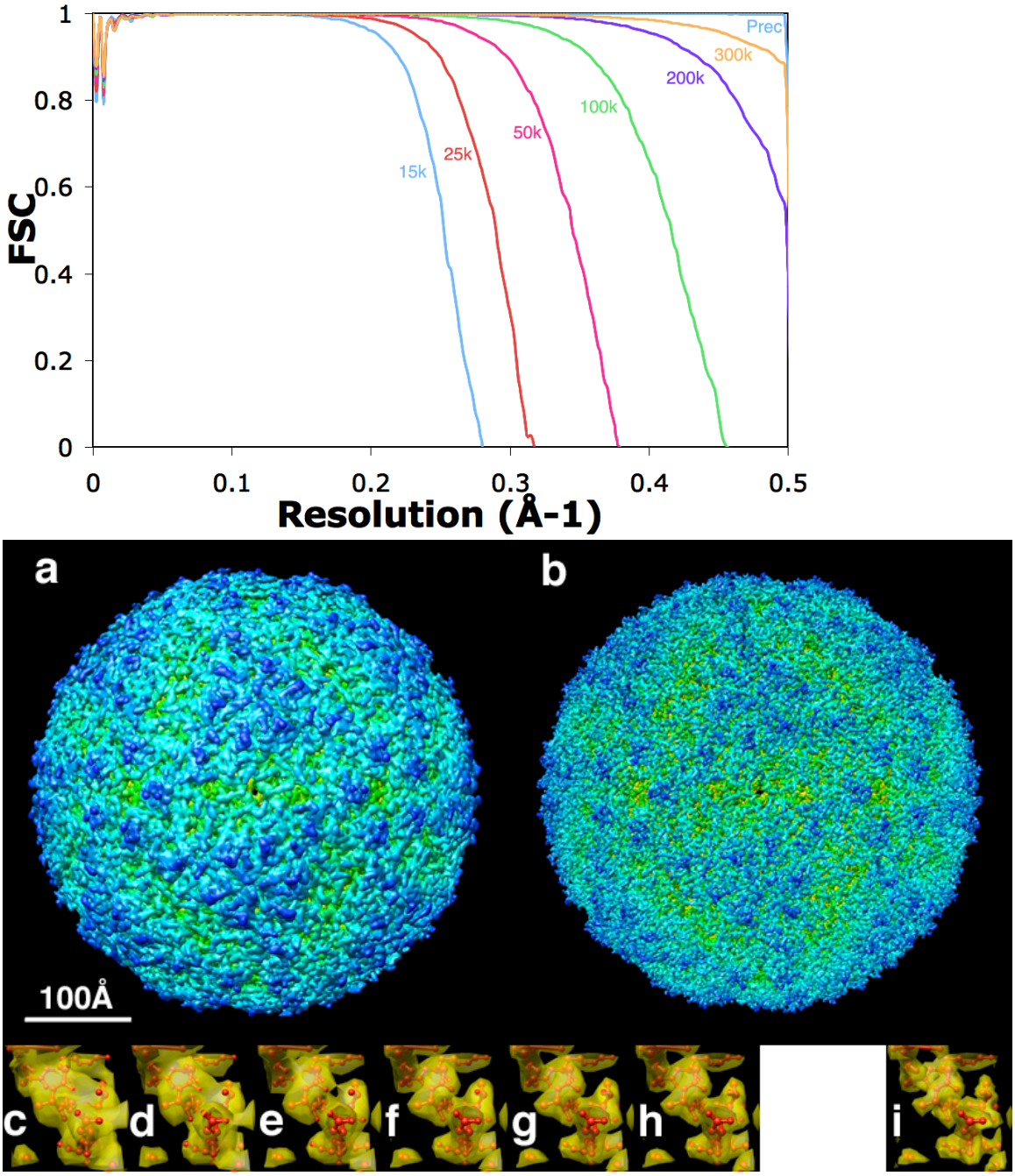

Figure 3-2. ***Prec* overcomes the curvature problem in Ewald projections.** (top) FSC curves for conventional Bsoft reconstructions of the foot and mouth virus from 5000 "Ewald projection" images simulated with the voltages shown, plus a reconstruction from the 15 kV images calculated by the *Prec* program, which completely corrects for the curvature problem. (a and b) Isosurface renderings of the conventional and *Prec* 15 kV reconstructions, respectively. (c, d, e, f, g, h) Transparent isosurfaces of a single α-helix from the 15, 25, 50, 100, 200, and 300 kV reconstructions, respectively, surrounding the atomic model used to simulate the images. (i) The same helix from the *Prec* 15kV reconstruction. FSC curves were calculated with *bresolve* (Heymann 2001) and isosurfaces were rendered with *Chimera* (Pettersen, Goddard et al. 2004)

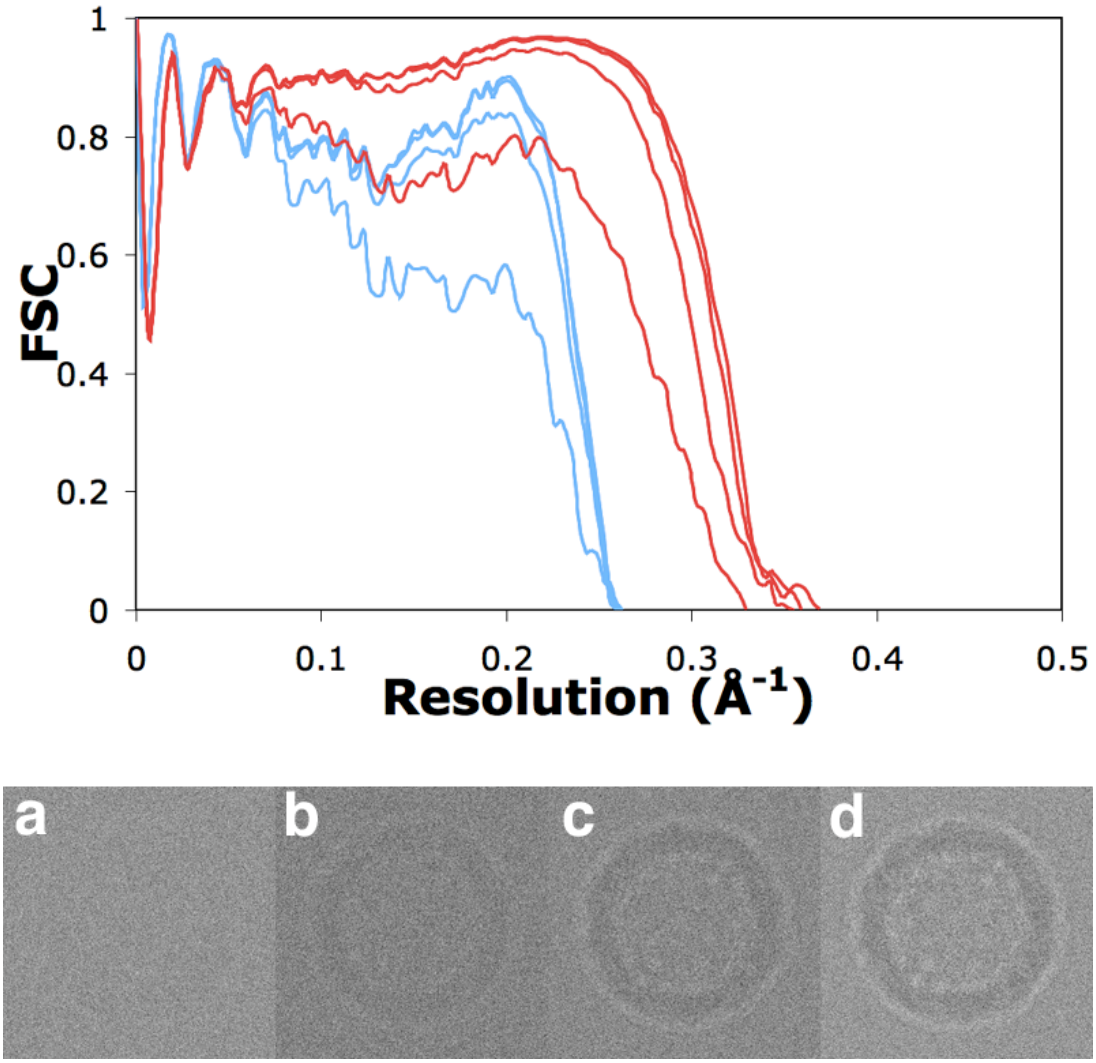

Figure 3-3. ***Prec*** **overcomes the curvature problem in multi-slice images and in the presence of noise**. (top) FSC curves reporting the resolution of reconstructions calculated using conventional methods (the IMIRS *reconstruct* program, blue) and *Prec* (IMIRS implementation, red) from 5000 fifteen-kV multi-slice images with SNRs of 0.001, 0.01, 0.05, and 0.1 (progressively with higher resolution). (a–d) One example multi-slice image for each noise level

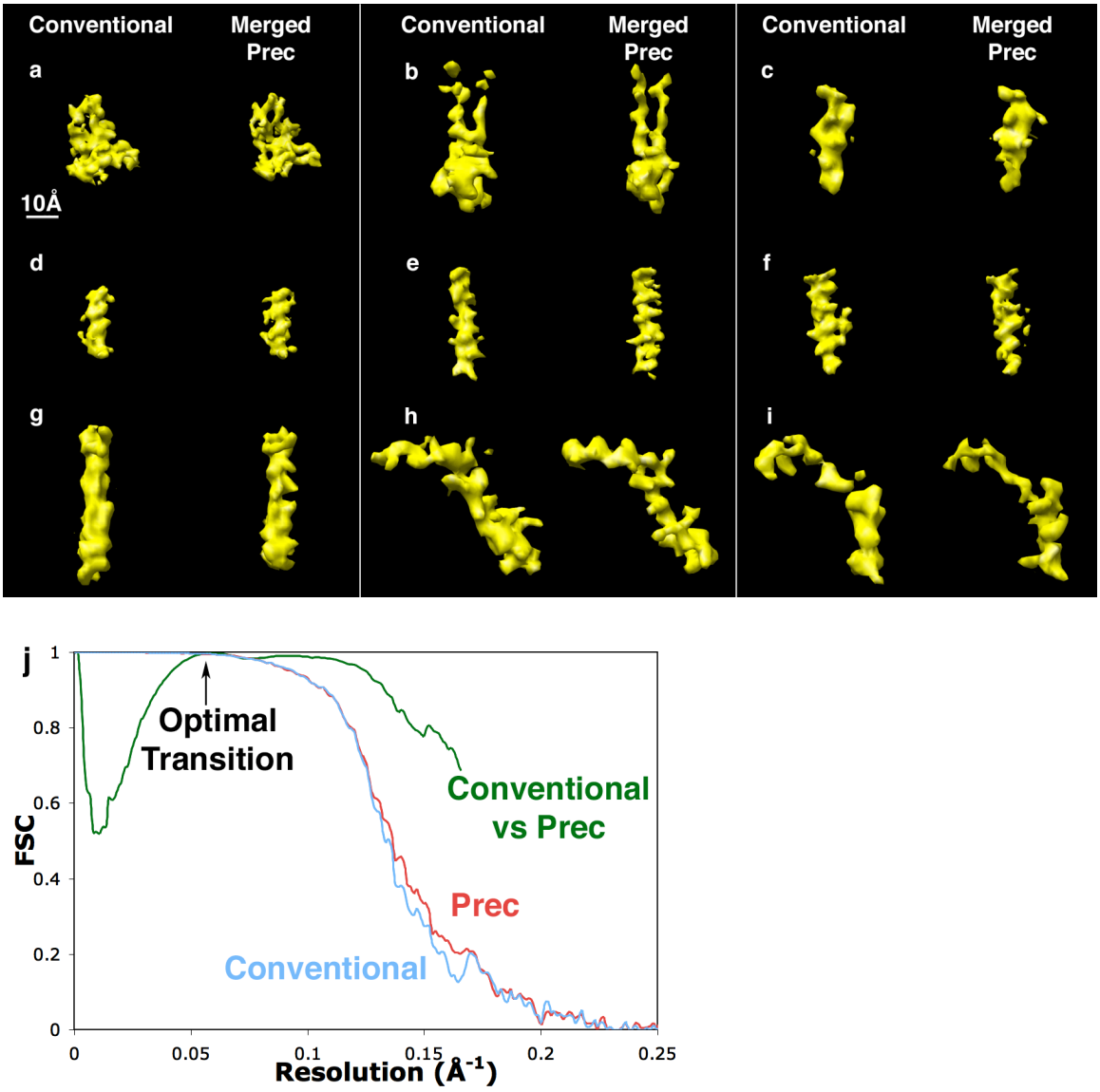

Figure 3-4. **Application of *Prec* to experimental images: 3D reconstruction of CPV.** (a–i) Isosurfaces of selected β-sheets (a, b) and α-helices (c–i) from the conventional and *Prec* reconstructions, respectively, do not clearly show improved interpretability of the *Prec* map. (j) FSC curves for the *Prec* (blue) and conventional (red) reconstructions of CPV, plus a third FSC curve (green) comparing the two that identifies the resolution at which *Prec*'s complex CTF-correction method becomes more appropriate than the conventional real CTF-correction

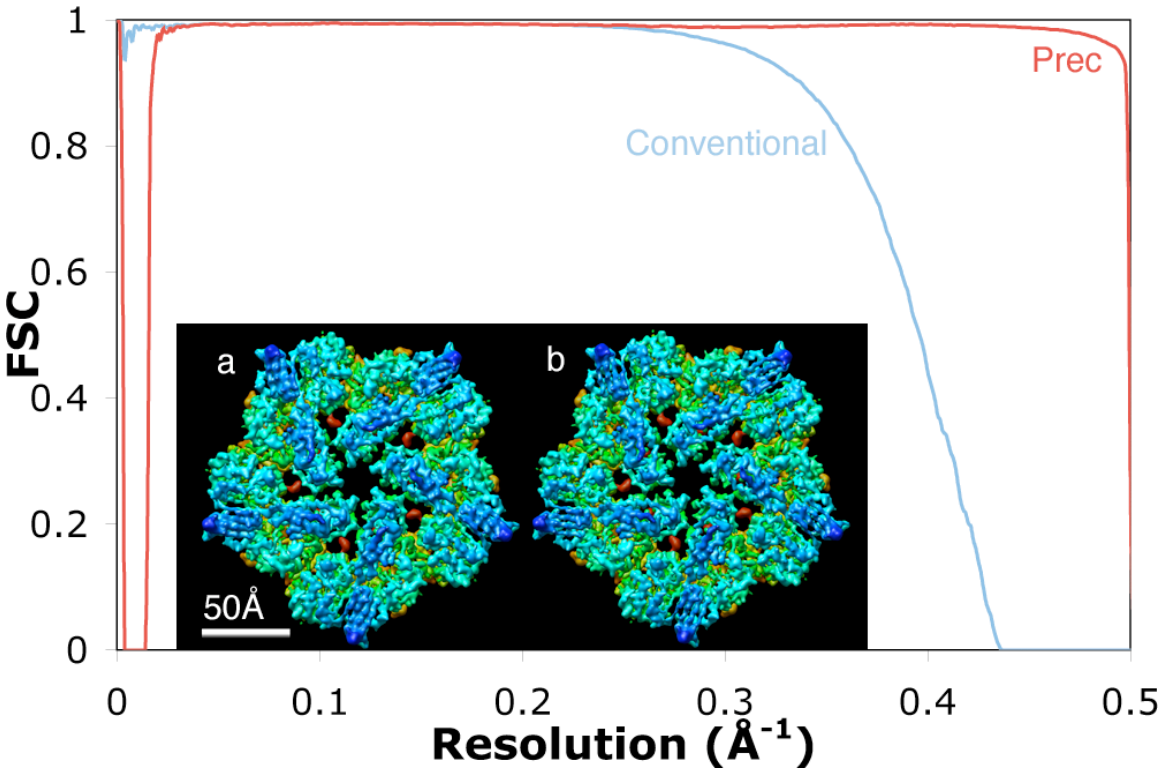

Figure 3-5. **Reconstructions of the 754 Å diameter Reovirus from 300 kV simulated images.** Curvature of the Ewald sphere does not limit the resolution of the conventional reconstruction (blue curve) until ~ 2.5 Å, showing that other factors must still be dominant in the recent experimental reconstructions of similarly sized viruses. *Prec* in EMAN eliminates the limitation, recovering the full resolution present in the simulated images. (a and b) Turrets from conventional and *Prec* (EMAN) reconstructions, respectively